energies

Article

Numerical Simulation of Flow and Heat Transfer of a Discontinuous Single Started Helically Ribbed Pipe

Simon Kügele [1,*], Gino Omar Mathlouthi [2], Peter Renze [1] and Thomas Grützner [3]

[1] Institute of Energy and Drive Technology, Ulm University of Applied Sciences, Albert-Einstein-Allee 53, 89081 Ulm, Germany
[2] Institute of Design and CA-Technology, Ulm University of Applied Sciences, Prittwitzstraße 10, 89075 Ulm, Germany
[3] Laboratory of Thermal Process Engineering, Institute of Chemical Engineering, Ulm University, 89081 Ulm, Germany
* Correspondence: simon.kuegele@thu.de

Abstract: In the present study, the turbulent flow field and the heat transfer in a single started helically ribbed pipe with a discontinuous rib are investigated. A large-eddy simulation (LES) technique is applied in a pipe section with cyclic boundary conditions. The aim of this study is to explain and further analyze the findings from the heat transfer measurements at such complex structures with the help of detailed flow simulations. The simulation results are validated with measurements at a Reynolds number of Re = 21,100 and a Prandtl number of Pr = 7 with water as fluid. The comparison clearly shows that the current method delivers accurate results concerning average flow field, turbulence quantities and local heat transfer. The results demonstrate that the applied method is capable of correctly simulating flows with heat transfer in complex three-dimensional structures. The overall heat transfer performance of the helically ribbed pipe with a discontinuous rib is compared to a smooth pipe and a continuous rib configuration. The impact of the interruption of the rib structure on pressure drop and heat transfer are analyzed in detail.

Keywords: large eddy simulation; pipe flow; heat transfer; ribbed tube

Citation: Kügele, S.; Mathlouthi, G.O.; Renze, P.; Grützner, T. Numerical Simulation of Flow and Heat Transfer of a Discontinuous Single Started Helically Ribbed Pipe. *Energies* **2022**, *15*, 7096. https://doi.org/10.3390/en15197096

Academic Editors: Artur Bartosik and Dariusz Asendrych

Received: 30 August 2022
Accepted: 22 September 2022
Published: 27 September 2022

1. Introduction

In order to improve the heat transfer in technical devices, pipes with a rough surface are used. In addition, there are many other possibilities to passively improve the heat transfer, for example various internals or the use of nanofluids, an overview of these methods can be found in the paper of Ajarostaghi et al. [1]. The roughness ensures that the boundary layer of the flow is disturbed, transport processes normal to the wall are enhanced, and, additionally, the heat transfer surface is increased. Due to larger frictional and pressure forces, the pressure loss is increased [2]. Most published studies of internally ribbed pipes are based on experimental methods. Due to the increasing computing power, it is now possible to perform detailed flow simulations. This enables an improved virtual product development to reduce the costs of expensive experiments and speed up the development.

In the past, numerous experimental studies have been performed on internally ribbed pipes. With the aim of improving heat transfer and pressure loss, helically ribbed pipes were investigated by Webb et al. [2], Gee and Webb [3], Withers [4,5], Han et al. [6], and Nakayama et al. [7]. These authors have established correlations for the heat transfer and the friction coefficient based on their experiments, which are valid for various physical and geometrical parameters. By applying measured data to a linear model, Ravigururajan and Bergles [8] developed general correlations for pressure loss and heat transfer in single-phase turbulent flow using the research data of Webb [9], Gee and Webb [3], Withers [4,5], and Kumar and Judd [10]. In addition, to develop correlations for heat transfer and friction in pipes with internal helical ribs, Zdaniuk et al. [11] used an artificial neural network approach based on experimental data.

For the investigation of internally structured pipes, the importance of simulations increases due to the ever increasing computing resources and the resulting reduced computing times. In the past, several studies have been performed in this area, and a selection of them are briefly described in the following.

A comparison between the experimental data of Ravigururajan and Bergles [8] with the results of Reynolds-averaged Navier–Stokes (RANS) simulations for a single started helically ribbed pipe can be found in Hossainpour and Hassanzadeh [12]. They show that it is possible to provide reasonably good results in the range of the Reynolds number from 25,000 to 80,000. In this study, no comparison of the local values such as the local heat transfer has been made. A comparison between RANS and a large-eddy simulation (LES) was performed by Vijapurapu and Cui [13]. Cauwenberge et al. [14] demonstrate that RANS simulations are unable to predict certain secondary flow phenomena that have an effect on heat transport and pressure loss. In the work of Wang [15], it has been shown by means of an LES simulation that the performance of helically corrugated pipes is superior to the transverse corrugated pipe. A multiple-started helically ribbed pipe is investigated in Akermann et al. [16] using an LES method, where the simulation setup is validated with experimental data for the Nusselt number and pressure drop for Reynolds numbers of 8000 and 16,000 and Prandtl numbers of 5, 7 and 9. Based on the previously mentioned experimental data from Mayo et al. [17], two studies have been carried out to validate a simulation with an LES model with the simpler continuous geometry. The first study was done by Cauwenberg et al. [18] and the second by Campet et al. [19]. Both studies show a good agreement between the simulation and measurement for the mean values of velocity and temperature. The authors were able to perform a successful validation for a continuous ribbed pipe geometry using an LES. The literature referenced above only deals with continuous structures at internal pipe walls. Measurements of three-dimensional structures were performed at the von Karman Institute, where Mayo et al. [17] determined experimentally the heat transfer and flow properties in a pipe with a helically structured rib. Further experiments for the identical pipe and a comparison with a modified version were performed in the publications of Virgillio et al. [20,21]. The flow and heat transfer between the ribs are investigated in these measurements and used for the comparison in the present study.

The aim of this study is to explain and further analyze the findings from these heat transfer measurements at such complex structures with the help of detailed flow simulations. Three-dimensional wall structures lead to very complex flow phenomena that have been rarely investigated so far. The experiments from the literature can usually only provide global values such as pressure loss and heat transfer, and local values can only be determined with complex measurement methods. With the current simulation method, it should be possible in the future to view the global results in connection with the local physical processes without complex measurement methods.

That is why in the present work an LES of a discontinuous single-started helically ribbed pipe is performed and validated with experimental data for the velocity and heat transfer between the ribs. The results demonstrate that it is possible to reproduce the measurement data even for complex geometries. The difficulty here is especially in the interruptions of the helix, so the local results are more difficult to compare than with a continuous helix. The aim of this study is to speed up the development process of new complex geometries and the associated correlations for the calculation of heat transfer and pressure loss.

2. Physical Modelling

The governing equations are given in the following section. The physical description of a turbulent flow with heat transport is based on the governing equation for mass, momentum and energy. The formulation used here is based on Anderson [22]. The continuity equation for a transient flow of a compressible fluid can be described as follows:

$$\frac{\partial \rho}{\partial t} + \nabla \cdot (\rho \mathbf{u}) = 0 \tag{1}$$

with the nabla-operator $\nabla = \left(\frac{\partial}{\partial x}, \frac{\partial}{\partial y}, \frac{\partial}{\partial z}\right)$, the density ρ, the velocity field $\mathbf{u}$ and time t.

The conservation of momentum is given by

$$\begin{aligned} \frac{\partial \rho \mathbf{u}}{\partial t} + \nabla \cdot (\rho \mathbf{u}\mathbf{u}) = -\nabla P + \rho \mathbf{g} + \\ \nabla \cdot \left(2\mu_{eff} \mathbf{S}(\mathbf{u})\right) - \nabla \left(\frac{2}{3}\mu_{eff}(\nabla \cdot \mathbf{u})\right) \end{aligned} \tag{2}$$

where P is the static pressure field and $\mathbf{g}$ is the gravitational acceleration. The effective viscosity μ_{eff} is the sum of molecular and turbulent viscosity. The rate of strain (deformation) tensor $\mathbf{S}(\mathbf{u})$ is defined as $\mathbf{S}(\mathbf{u}) = \frac{1}{2}\left(\nabla \mathbf{u} + (\nabla \cdot \mathbf{u})^T\right)$.
The conservation of energy in the fluid is defined in terms of the specific enthalpy h as

$$\begin{aligned} \frac{\partial(\rho h)}{\partial t} + \nabla \cdot (\rho \mathbf{u} h) + \frac{\partial(\rho k)}{\partial t} + \nabla \cdot (\rho \mathbf{u} k) - \frac{\partial P}{\partial t} = \\ \nabla \cdot \left(\alpha_{eff} \nabla h\right) + \rho \mathbf{u} \cdot \mathbf{g} \end{aligned} \tag{3}$$

where $k = \dfrac{|\mathbf{u}|^2}{2}$ is the specific turbulent kinetic energy. The effective thermal diffusivity α_{eff} is defined as the sum of laminar and turbulent thermal diffusivity

$$\alpha_{eff} = \frac{\rho \nu_t}{Pr_t} + \frac{\mu}{Pr}, \tag{4}$$

where Pr is the Prandtl number, Pr_t is the turbulent Prandtl number and ν_t is the turbulent kinematic viscosity.

To predict the effects of turbulence, the turbulent transport parameters require a turbulence model. In this work, the LES method is used to take turbulence into account. A RANS is clearly not suitable for the analysis of near wall turbulent transport phenomena. Since the use of a DNS significantly exceeds the computational effort of the LES, such a method is applied. Here, the large eddies, which contain most of the turbulent energy, are resolved by the conservation equations and only the small eddies are modeled. A filter function with a characteristic filter width of $\Delta = (\Delta_x \Delta_\omega \Delta_r)^{(1/3)}$ is applied to the conservation equations. This filter function splits up any field variable ϕ in a resolved $\hat{\phi}$ and non-resolved (subgrid) part ϕ' [23]. Following the Boussinesq approximation, the viscosity is replaced by an effective viscosity, which is the sum of molecular viscosity and the viscosity of the subgrid scales (eddy-viscosity), $\nu_{\mathrm{eff}} = \nu + \nu_{\mathrm{SGS}}$. The subgrid scale viscosity can then be modeled as $\nu_{\mathrm{SGS}} = C_{\mathrm{k}} \Delta \sqrt{k_{\mathrm{SGS}}}$, where $C_{\mathrm{k}} = 0.07$ is a model constant and k_{SGS} is the kinetic energy of the subgrid scale. The 0-equation WALE [24] (wall-adapting local eddy-viscosity) model calculates the kinetic energy of the subgrid scale using the following equation:

$$k_{\mathrm{SGS}} = \left(\frac{C_{\mathrm{w}}^2 \Delta}{C_{\mathrm{k}}}\right)^2 \frac{\left(S_{\mathrm{ij}}^{\mathrm{d}} S_{\mathrm{ij}}^{\mathrm{d}}\right)^3}{\left(\left(\overline{S}_{\mathrm{ij}} \overline{S}_{\mathrm{ij}}\right)^{5/2} + \left(S_{\mathrm{ij}}^{\mathrm{d}} S_{\mathrm{ij}}^{\mathrm{d}}\right)^{5/4}\right)^2}. \tag{5}$$

where S_{ij} is the strain rate tensor of the resolved scale, $C_{\mathrm{w}} = 0.325$ and $C_{\mathrm{k}} = 0.094$ are model constants. This model takes into account the rotation of the flow field, so an additional damping function for ν_{SGS} in the near wall region is not necessary. Most of the turbulent energy is in the large eddies and these are difficult to model with a turbulence model because of their individual structure. Thus, the modelling part is very small compared to RANS.

OpenFOAM® (Open Source Field Operation and Manipulation) in the version of v1812 with the *buoyantPimpleFoam* solver was chosen for this study.

3. Geometry and Reference Cases

The validation reference case is based on experimental data published in the literature. The experiments were conducted at the "TU - Heat and Mass Transfer Laboratory" at the von Karman Institute in Sint Genesius Rode, Belgium. The flow data are taken from Virgilio et al. [20] and the heat transfer data from Virgilio et al. [21]. For the velocity measurements, a low-speed water tunnel was used. The measurement setup is configured in a way that the pressure at the inlet can be assumed to be constant; for a full optical access, the pipe is made of acrylic glass. Two different helical turbulators are measured, defined as RIB-1 and RIB-2, illustrated in Figure 1. The RIB-1 is the continuous helicoidal turbulator studied by Mayo et al. [17]. These are made of acrylonitrile butadiene styrene using a 3D printer. The diameter D of the pipe examined here is 150 mm; in the experiment, the pipe length is 15 × D. The rib pitch p corresponds to 63 mm, rib height e is 5.4 mm, angle between the axial and helix-wise directions is 80°, and the rib width is 10.8 mm. RIB-2 is different in that the height of the semi-circular rib changes along the helical pattern direction, but the maximum height remains the same for both ribs. After an angular displacement of 11°, this height becomes zero in both directions of the helix. This results in six obstacles on one pitch of the helix, with a total of nine pitches. For RIB-1 and RIB-2, Reynolds numbers of 24,400 and 21,100 have been investigated in the simulation. The stereoscopicv particle image velocimetry (S-PIV) images are taken between the seventh and eighth pitch. Data are only available in the area between the ribs. Liquid Crystals Thermography (LCT) is used to measure the stationary heat transfer. To reduce the angular influence on the measurement inaccuracy, a lately developed calibration technique for the narrow-band LCT was successfully applied. Since the simulations are computationally expensive and RIB-1 has already been examined in detail by Campet et al. [19] and Cauwenberg et al. [18] with an LES, in this article, RIB-2 has been investigated with the use of LES.

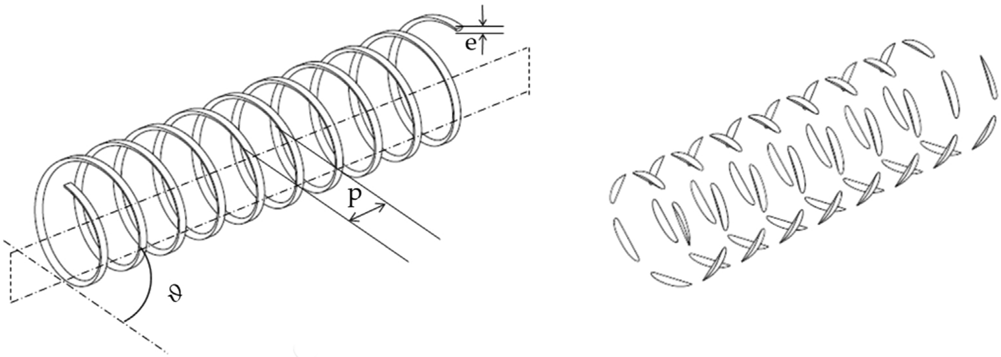

Figure 1. Schematics of the continuous helicoidal turbulator RIB-1 (**left**) and RIB-2 (**right**) from Virgillio et al. [20].

4. Numerical Methodology

The accurate calculation of heat transfer in turbulent pipe flow requires a fully developed turbulent flow inside the pipe. Limitations of computational resources did not allow simulations of a long pipe to ensure a fully developed flow. By simulating a small section of a pipe with cyclic boundary conditions at the inlet and outlet, a fully developed turbulent flow could be achieved, if a sufficient number of flow cycles were carried out. Table 1 lists the boundary conditions used, and the schematic illustration is shown in Figure 2. For the calculation, it is necessary to insert a source term for momentum and the energy equation due to the cyclic boundary conditions. This setup is also applied in the studies by

Campet et al. [19], Kügele et al. [25] and Akermann et al. [16]. Second-order methods are used for all discretisations. A Courant number of 0.3 is used for the computation, and, after a quasi-steady state of the flow has set in, the results are averaged over seven cycles as in the study by Campet et al. [19].

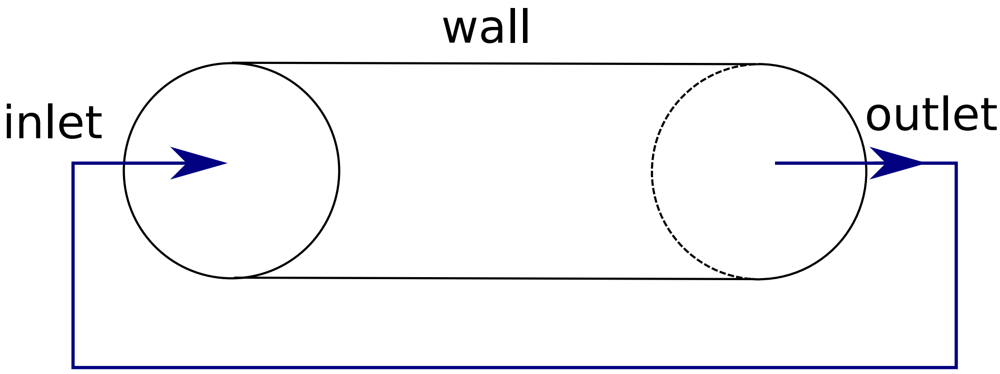

Figure 2. Schematic representation of the boundary conditions used.

Table 1. Definition of the boundary conditions used.

	U	**p**	**T**
wall	$\mathbf{u} = \mathbf{0}$	$\partial p/\partial n = 0$	$\partial T/\partial n = -10{,}000$
inlet	cyclic	cyclic	cyclic
outlet	cyclic	cyclic	cyclic

The length of the calculation area is 4 $\times$ D. For the cyclical boundary conditions, it must be ensured that inlet and outlet are exactly identical. The mesh without the boundary layers is created with cfMesh; snappyHexMesh is then used to generate the final mesh. The maximum cell size within the geometry is 0.002 mm. Near the wall, the grid resolution is reduced to about 0.0005 mm to be able to better represent the structure of the ribs and to keep the transition between layers and cells small. The number of cells adds up to 23.33 million, with 67% of the cells forming the layers. The total number of layers used is ten, the smallest layer has a height of 0.03116 mm, and the growth rate of the layers is set to 1.2. The influence of the refinement on the wall and the addition of layers can be seen on the inlet and on the ribs in Figure 3. With these techniques, a y^+ value of less than 0.2 can be achieved. The values for x^+ and z^+ correspond to 7, which is sufficient for LES as shown in Akermann et al. [16].

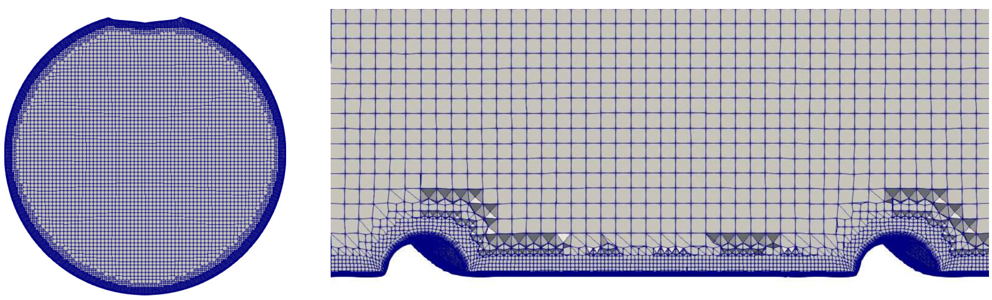

Figure 3. Display of the grid with layers at the inlet (**left**) and along the center (**right**) of the rib in RIB-2 geometry.

To ensure a sufficient grid resolution for the LES, the LSR (Length Scale Resolution) parameter is investigated. It corresponds to the ratio between the actually resolved energy level and the corresponding lower limit of the inertial subrange and is defined as:

$$LSR = \frac{\Delta}{60 \cdot \eta_{kol}} \tag{6}$$

where Δ corresponds to the grid width. The Kolmogorov length scale is calculated with:

$$\eta_{kol} = (\frac{\nu^3}{\epsilon})^{1/4} \tag{7}$$

$$\epsilon = \frac{k^{3/2}}{D/6} \tag{8}$$

and the turbulent kinetic energy k is determined using the simulation results. If the value is equal to 1, the turbulent scales are resolved up to the dissipation range. Therefore, a link between resolved energy levels and the local filter sizes can be created [26]. The evaluation in Figure 4 shows that the value is below 1 in all ranges. This ensures that the grid resolution is high enough.

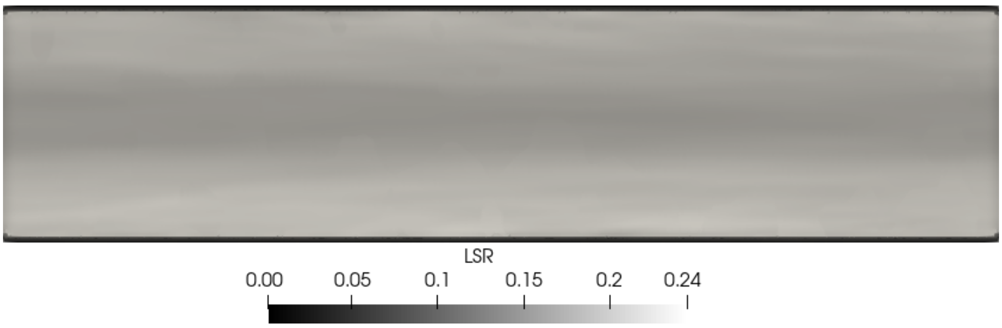

Figure 4. Display of the grid with layers at the inlet of the RIB-2 geometry.

5. Flow Field Analysis

A Reynolds number of 21,100 and a Prandtl number of 7 has been chosen for the simulation, the operating fluid is water and the thermophysical properties are constant. To validate the simulation results, the flow field is analyzed in a range between 40 and 100 percent of the inner radius to focus on the near wall area. First, the velocity profiles calculated by the simulations are compared with the experimental data. All velocities are averaged with U_0, where for the variance U_0^2 is applied. The results in Figure 5 show that the simulation can reflect the measured values both in the area near the wall and towards the centre. For the first two velocity profiles, the values of simulation and measurement near the wall falls below zero, which is an indication of the backflow being correctly reflected by the model. The maximum velocity is 1.4 times the bulk velocity.

The investigation of the azimuthal velocity in Figure 6 also shows a good agreement with the measured values. The deviation of simulation and measurement is less than 10%. Especially at the first two measurement lines after the rib, the deviation between simulation and measurement is relatively high. Here, because of the flow recirculation, the averaging in simulation and measurement is very sensitive to pertubations and therefore susceptible to errors. Due to the detachment of the flow and the resulting backflow after the rib, the maximum velocity at the first measurement lines is lower compared to the measurement lines directly before the rib. Thus, the maximum value of the first curve is 0.069 compared to 0.143 at the last curve, which is an increase of 48%. Furthermore, in simulation and experiments, the azimuthal velocity above the ribs approaches zero. From this, it can be concluded that the described effects only occur close to the wall.

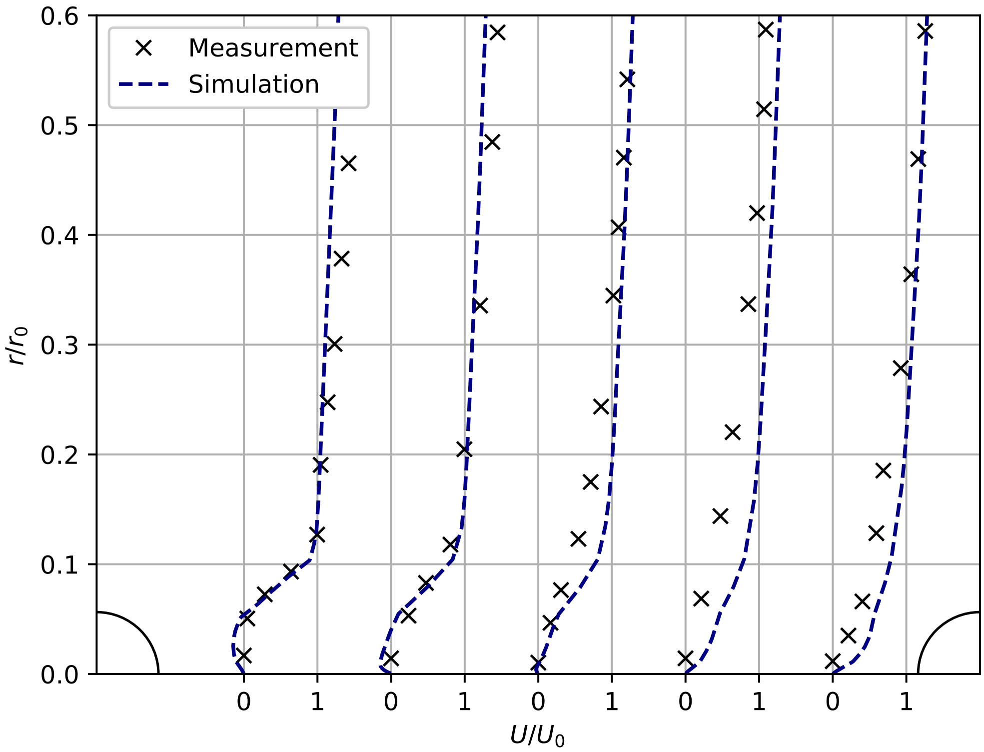

Figure 5. Comparison between measurement and simulation with the velocity in the flow direction.

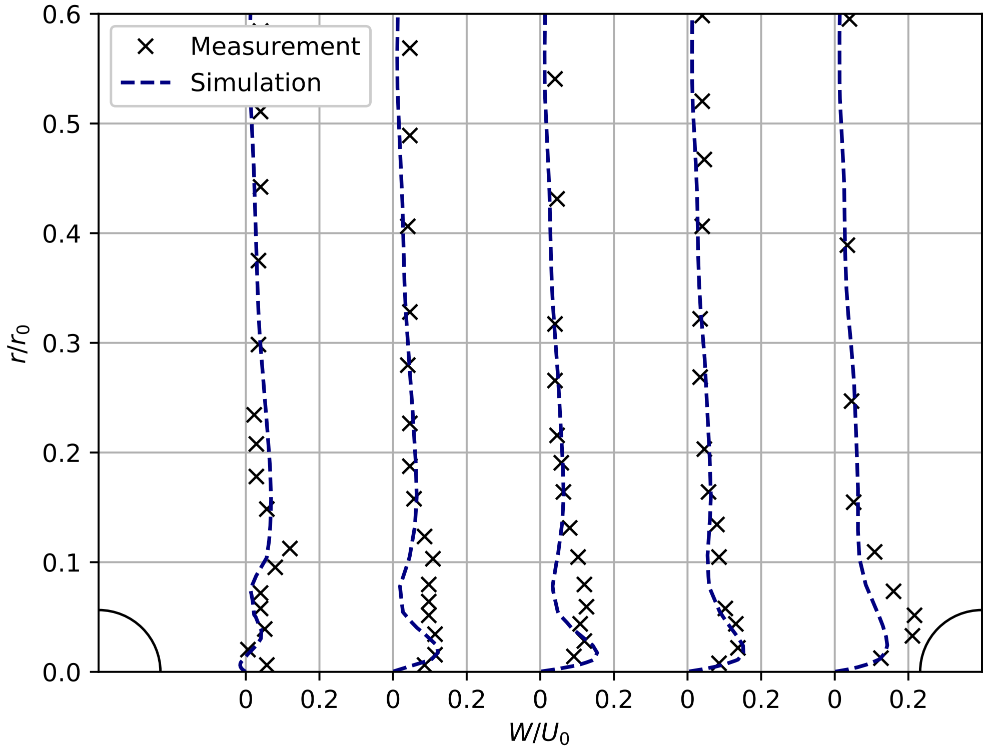

Figure 6. Comparison between measurement and simulation with the velocity in the circumferential direction.

The variance <*uu*> in the modelled and measured flow shows a good agreement as shown in Figure 7. The greatest deviation is seen in the first two curves. Here the variance is significantly lower than in the experimental data. The maximum value is 43% smaller at the first curve and 13% smaller at the second curve. It is assumed that the complex structures, caused by the detachment of the flow, are responsible for this difference. Nevertheless, the measurements can be replicated with the simulation. The comparison in Figure 8 for <*uv*> also shows a good agreement in this case. Overall, the simulation is able to reproduce the measurements for both the velocity profiles and the turbulent fluctuations well. Therefore, the simulation model is able to reproduce the turbulent flow in a ribbed pipe and is suitable for further investigations of the flow.

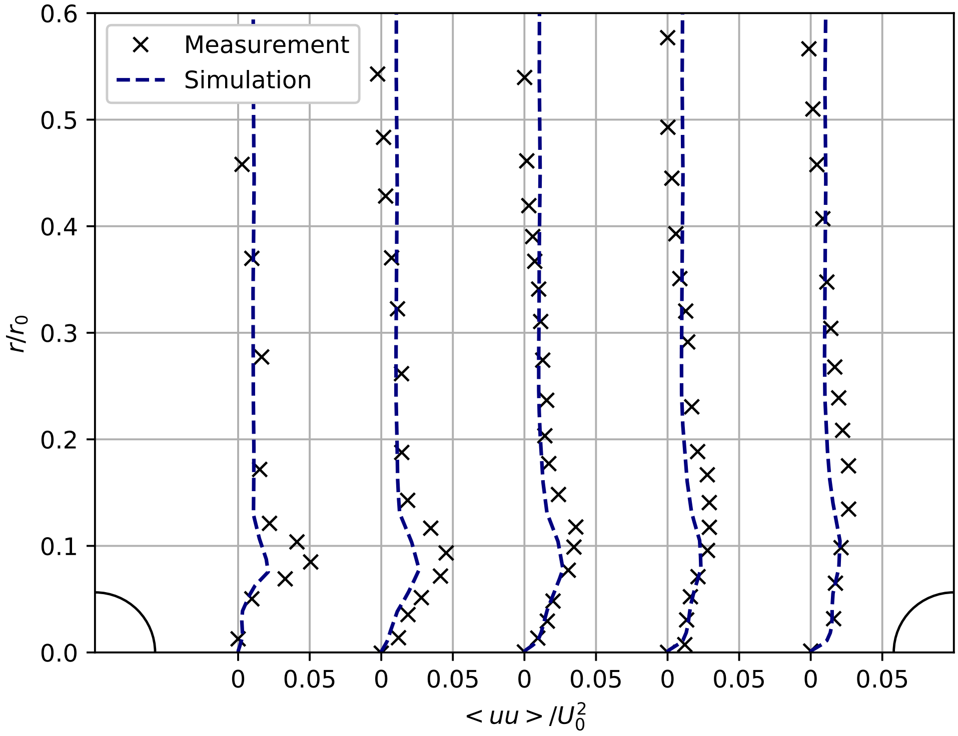

Figure 7. Comparison between measurement and simulation with the velocity variations <*uu*>.

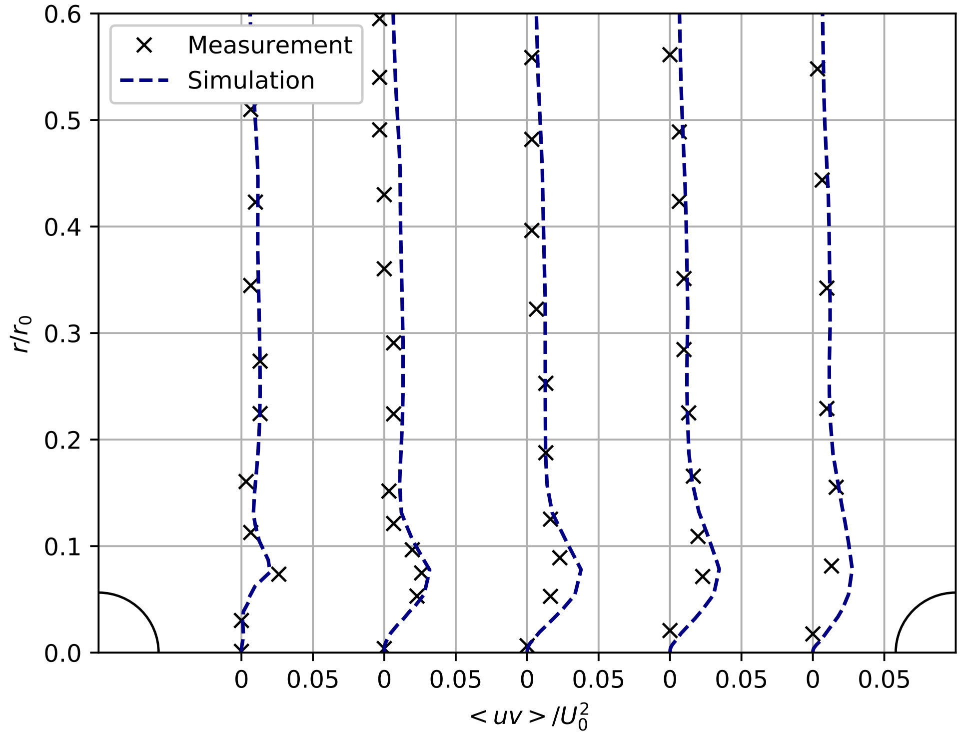

Figure 8. Comparison between measurement and simulation with the velocity variations <*uv*>.

6. Heat Transfer Analysis

For heat transport, the turbulent kinetic viscosity plays a major role, as can be seen from Equation (4). Especially near the wall, the heat transfer is dominated by the thermal diffusivity, while it can be neglected in the main flow. In the main flow, the thermal diffusivity has a negligible contribution compared to the turbulent transport. In order to be able to neglect the turbulent Prandtl number in the modeling approach, the ratio of molecular to turbulent viscosity is examined in Figure 9. From the results, it can be seen that the turbulent kinetic viscosity ν_t near the wall area is approaching zero, since the resolution of the mesh is very high here. This relationship can be explained by the following equation which is used for the calculation of ν_t:

$$\nu_t = (C_S \Delta)^2 \mathbf{OP}. \tag{9}$$

where Δ is the cell width, C_S is a model constant and **OP** is the LES model operator. The strong increase at $y/r \approx 0.05$ can be explained by the quadratic relationship of the cell width. Since the cells in this range become larger, the value of ν_t increases as can be concluded using Equation (9).

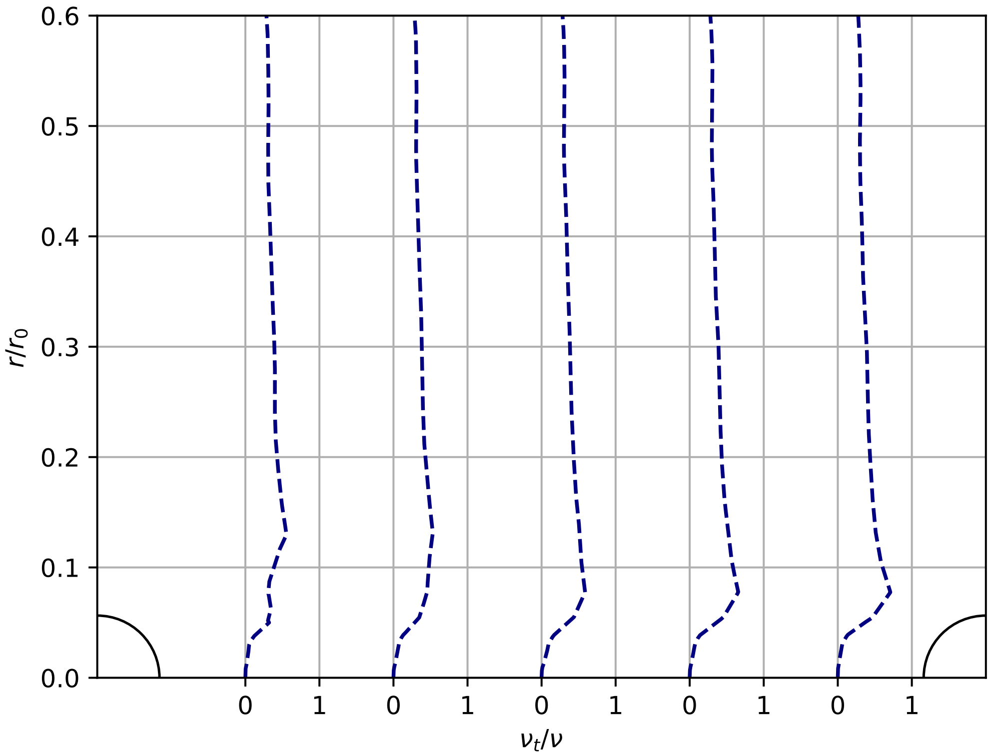

Figure 9. Representation of the turbulent viscosity in relation to the molecular viscosity.

In Figure 10, the measured Nusselt number is compared with the results of the simulation. The relationship between the Nusselt number of the examined structure and a smooth pipe is displayed. This ration is defined as EF with:

$$EF = Nu/Nu_S, \tag{10}$$

where Nu_S is calculated with the Dittus–Boelter correlation [27]:

$$Nu_S = 0.023 \cdot Re^{0.8} \cdot Pr^{0.4} \tag{11}$$

Measurements can only be made for the area between the ribs, and a detailed explanation can be found in Virgillio et al. [21]. The grey area corresponds to the tolerance range of the measurement errors. For a better overview, this representation is used instead of error bars. The comparison shows a very good agreement between the simulation and the measurement, except for the area directly before and after the rib. Investigations by Campet et al. [19] were able to demonstrate that, analogous to the results of this research, the deviation between simulation and experiment are significantly higher at these points. It can therefore be assumed that a measurement of the correct values for the heat transfer at these points is critical.

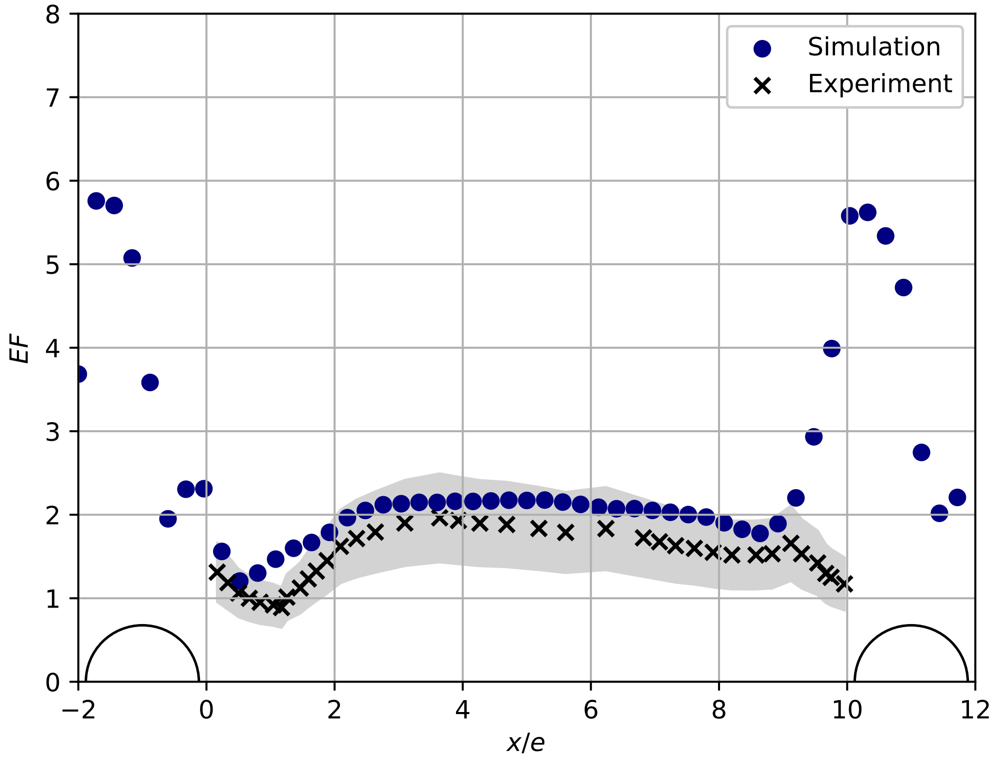

Figure 10. Comparison between measurement and simulation of the Nusselt number in relation to the smooth pipe between the ribs; the grey area shows the maximum and minimum values of the measurement.

As previously proven in Mayo et al. [17], there is a local maximum for the Nusselt number between two ribs along the axial flow direction in the pipe, from the point where the flow is reattached. This can be determined by evaluating the wall shear stress τ_x in the flow direction. In Figure 11 , τ_x is displayed in the range $x/e = 2$ and 8, and the reattachment point is located at the point where the value of τ_x changes its sign. It can thus be determined at $x/e \approx 5.05$. The local maximum of EF between the ribs, shown in Figure 12, is located in the same area. This is caused by the cold fluid transported from the bulk flow in wall direction, thus resulting in a higher temperature difference between wall and fluid. This increase is linear in relation to the Nusselt number. After the reattachment of the flow at $x/e \approx 5.05$, the Nusselt number becomes smaller again.

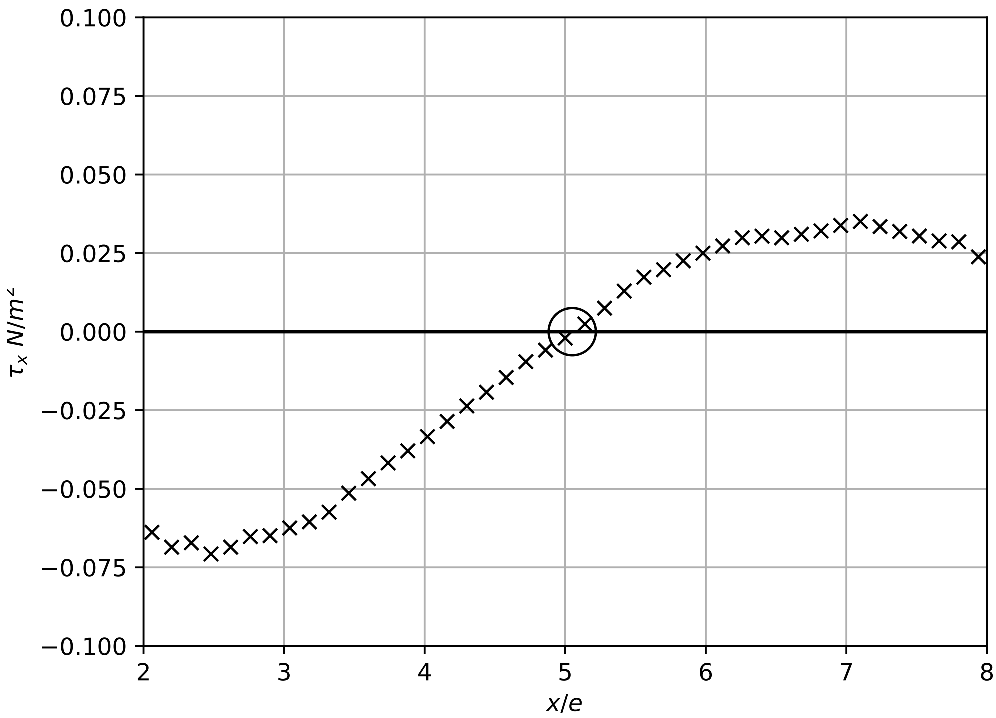

Figure 11. Representation of τ_x to determine the reattachment point of the flow after detachment at the rib.

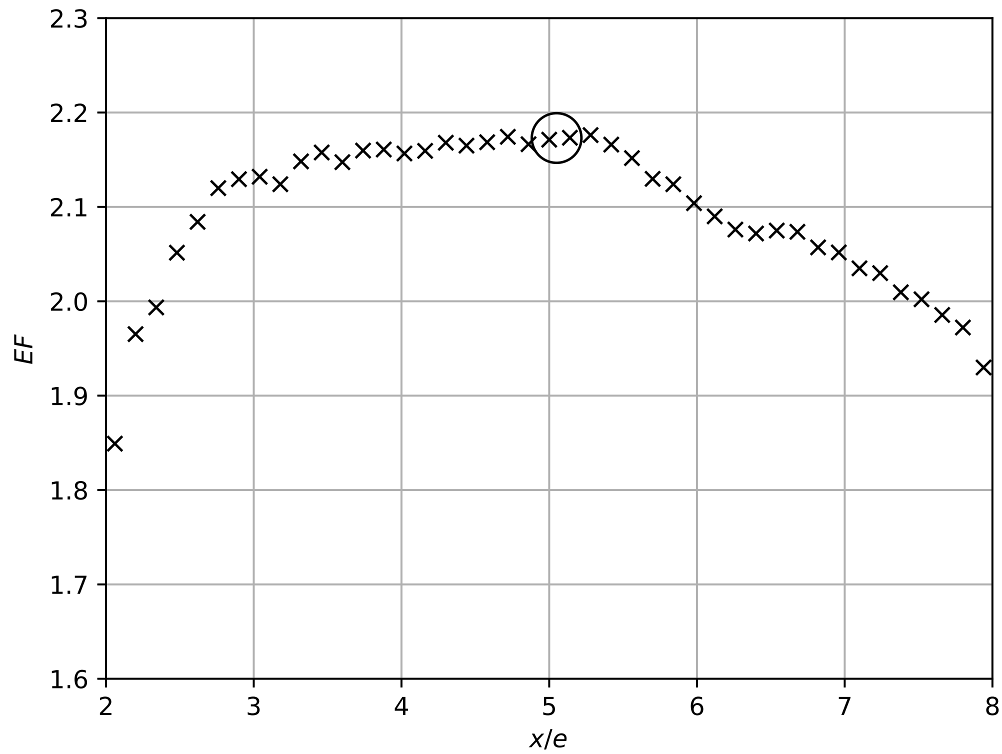

Figure 12. Display of the Nusselt number in the range from $x/e = 2$ to $x/e = 8$ to show the influence of the reattachment point of the flow on the Nusselt number.

For RIB-1, a reattachment point of the flow at $x/e \approx 4.25$ has been determined in Virgilio et al. [20]. The author points out that the reattachment point of the flow for RIB-2 is located further upstream than with RIB-1, which can be confirmed by the results shown here. The authors state that the interruptions of the helix prevent the flow from a blockage in comparison to the geometry in RIB-1. Using Figure 13, it can be illustrated with the streamlines that the fluid can also flow around the interrupted rib.

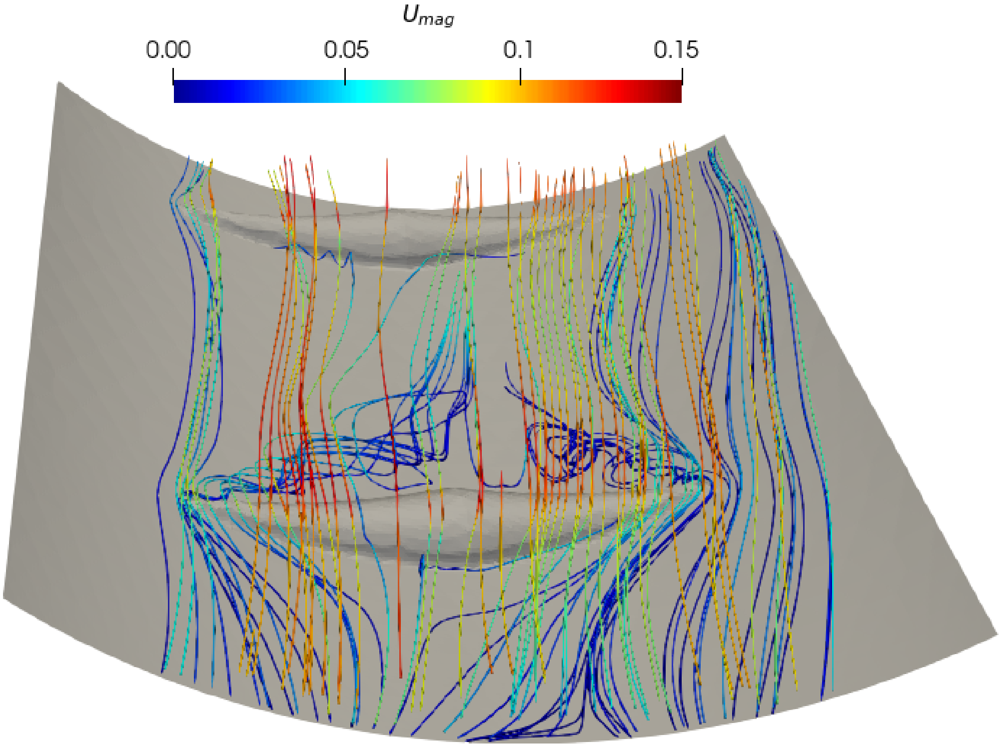

Figure 13. Streamlines of the magnitude velocity, over an interrupted rib.

The analysis of EF in Figure 14 demonstrates that an increase in efficiency compared to the smooth pipe is achieved almost everywhere, with the exception of the region highlighted in orange. In contrast to the RIB-1 with a continuous corrugation, the interruption and reduction at the sides results in reduced global heat transfer. Because the area in front of the centre of the rib before the flow separates has the highest heat transfer, and this area becomes smaller on both sides with this kind of geometry. The global value of EF for the measurement is 1.44 ± 0.41 for a Reynolds number of 21,160. In the simulation, the average value is 1.75 for a Reynolds number of 21,100 and is therefore still within the tolerance range of the measurement. Compared to the simulation of the RIB-1 geometry at a Reynolds number of 20,000, the value for EF decreases by 32%, showing that the interruption of the ribs reduces the heat transfer.

To compare the performance of the structured pipe with a smooth pipe, the performance evaluation factor (PEC) is used, defined as:

$$PEC = \frac{Nu/Nu_S}{(f/f_S)^{1/3}} \tag{12}$$

Nu, f, Nu_S and f_S are the Nusselt number and the friction factor of the investigated geometry and the ones of a smooth pipe (index S). To calculate the friction factor, the correlation of Gnielinski [28] is applied. If the value of the PEC factor is higher than 1, the improvement of the heat transfer is greater than the increased costs due to the pressure loss. A PEC factor of 1.53 is determined for the pipe examined here. Thus, it can be shown that the additional heat transfer is higher than the additional loss due to the additionally required pump power.

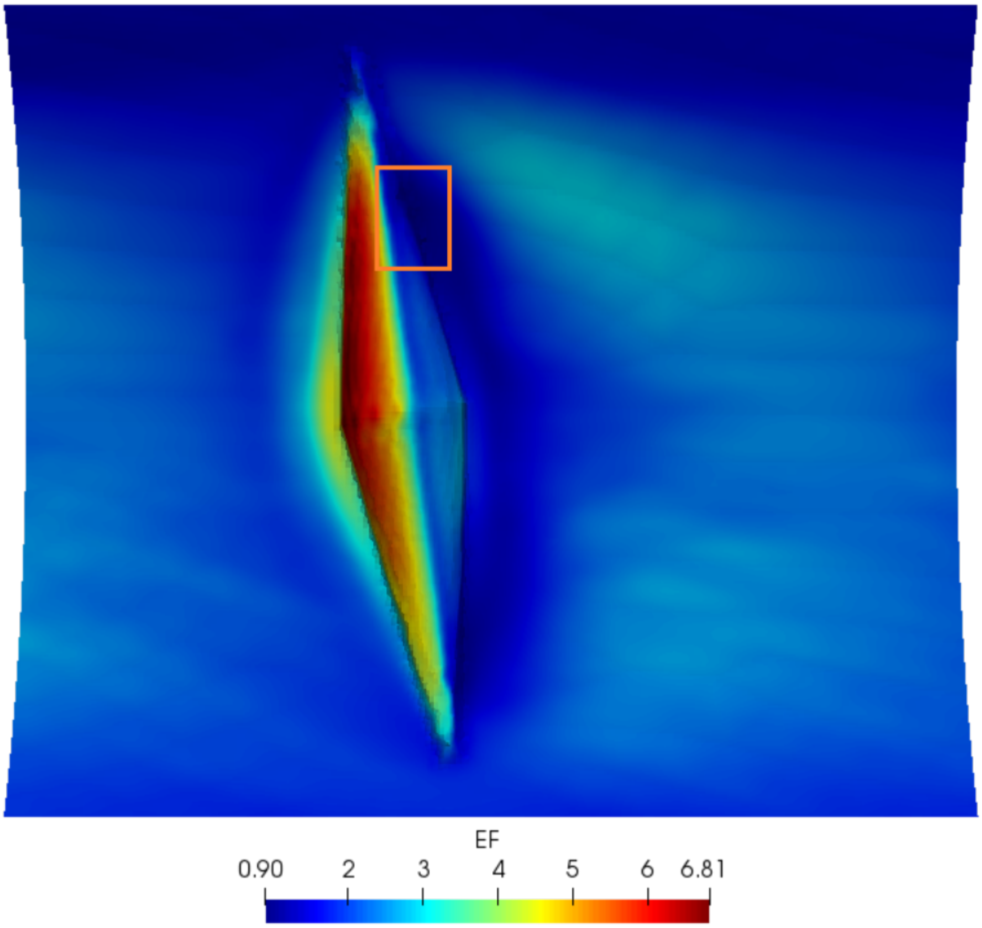

Figure 14. Representation of the ratio of Nusselt number to Nusselt number smooth pipe over a complete rib.

7. Pressure Loss

The experiments do not provide local pressure data; therefore, the results are compared with the values of the LES for RIB-1 from Campet et al. [19]. Here, the local friction coefficient C_f and the pressure coefficient P_{Norm} from Equations (13) and (14) are compared. A derivation of the two coefficients is provided by Campet et al. [19]. C_F has been validated in the above-mentioned paper using measurement data between the ribs and is defined as follows:

$$C_f = \frac{\tau_x}{0.5 \cdot U_0^2 \cdot \rho} \tag{13}$$

with the bulk velocity U_0 and the wall shear stress τ_x in the flow direction. The pressure coefficient P_{norm} is defined with:

$$P_{norm} = \frac{P - P_{ref}}{0.5 \cdot U_0^2 \cdot \rho} \tag{14}$$

where P_{ref} corresponds to the pressure on the wall at $x/e = 0$, so P_{norm} becomes zero at this point. Figure 15 shows the comparison between the two rib structures for C_f in the centre of the interrupted rib. It can be seen that the change of sign of C_f takes place where the reattachment point of the flow is located. This is caused by the velocity gradient being directly included in the calculation of τ_x. Furthermore, there is a backflow at RIB-2 shortly before the rib shown in Figure 16, which causes τ_x to obtain a negative value. This swirling is not visible at RIB-1, as can be concluded from the results of Campet et al. [19].

In addition to that, the peak in the simulation of RIB-2 is clearly above the values of RIB-1 and the maximum of the first mentioned geometry is 0.0686 compared to 0.0185, which corresponds to an increase of 370%. It is assumed that the velocity gradient on the rib due to the backflow in front of the rib results in a strong increase in local velocity.

The global C_f value used to calculate the pressure drop in the Darcy–Weißbach equation has a value of 0.0167 for RIB-2 and 0.0304 for RIB-1. The pressure drop in the geometry examined here is therefore lower by a factor of 1.82, since the influence of C_f is directly linear in the equation for the global pressure loss.

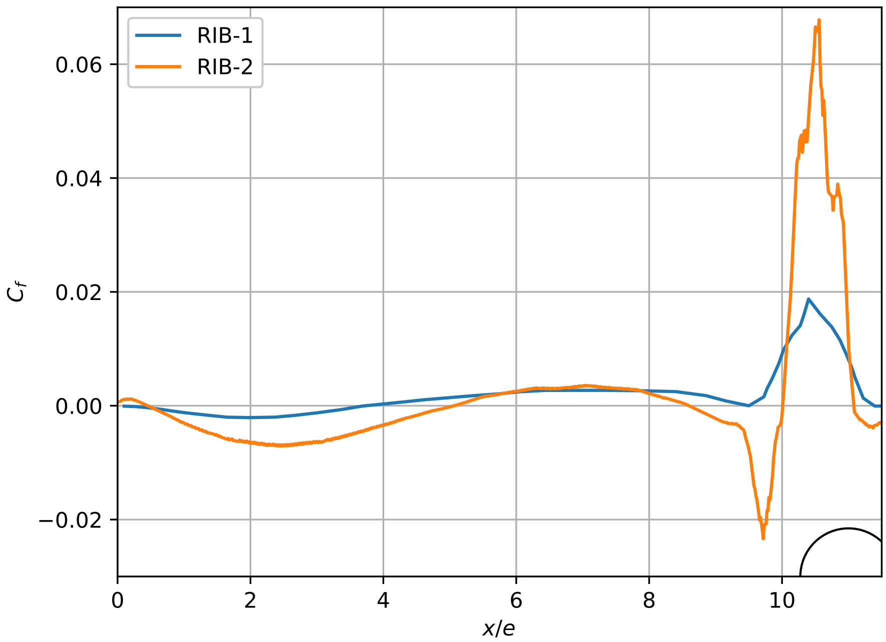

Figure 15. Comparison of the values of C_f between RIB-1 with values from Campet et al. [19] and RIB-2.

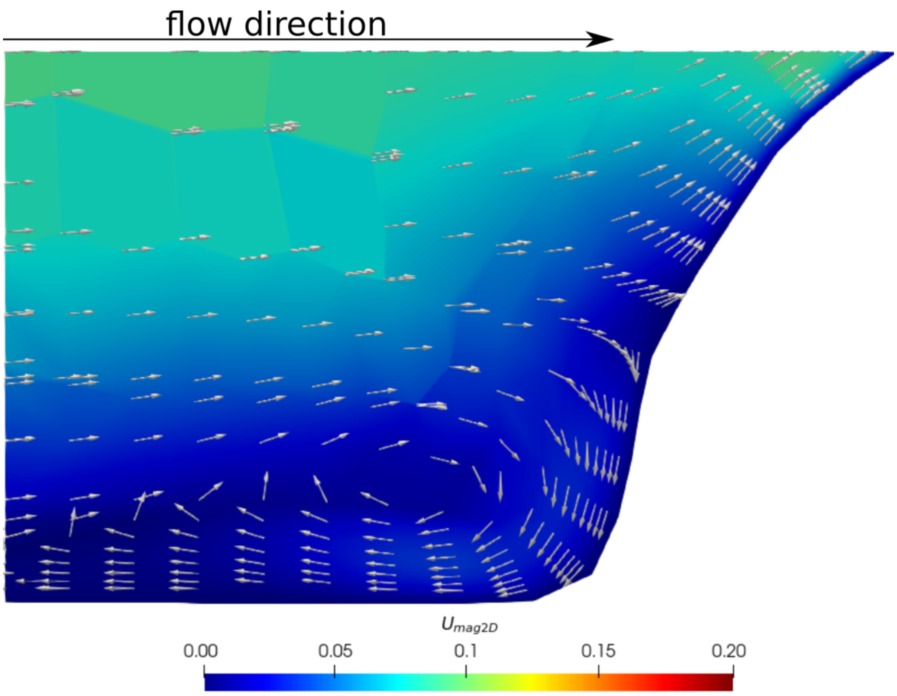

Figure 16. Two-dimensional velocity combined with vector arrows in front of the rib to show the backflow that takes place there.

Figure 17 compares the pressure coefficients over the centre of the interrupted rib. The maximum value in the range at x/e = 10, shows that the pressure coefficient is almost identical. The pressure coefficient of RIB-1 is almost always above RIB-2 in the positive range and below RIB-2 in the negative range. While the flow has to pass over continuous rib structure at RIB-1, it is partly redirected through the gaps in the interrupted rib at RIB-2, which explains the differences in the pressure coefficient plot.

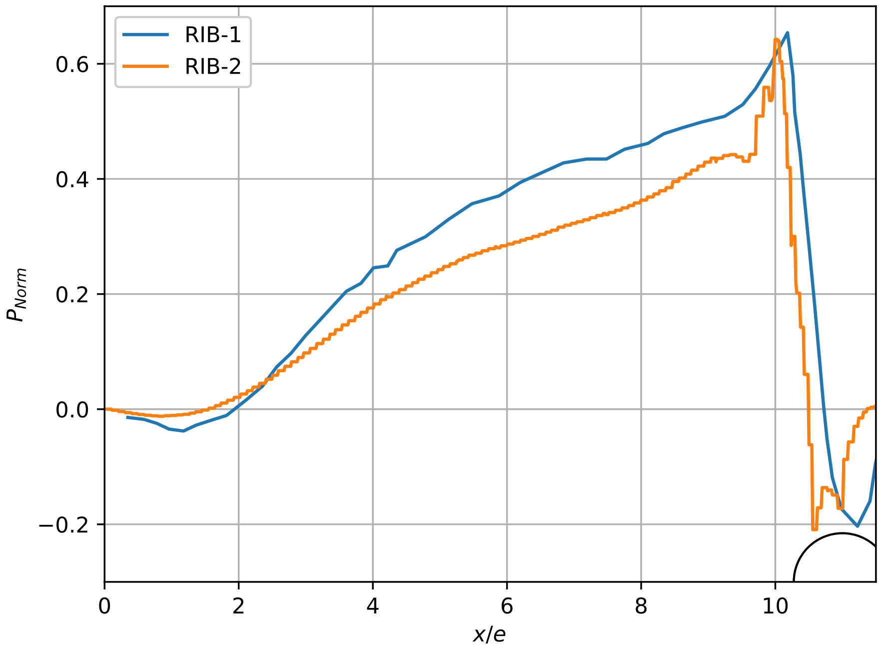

Figure 17. Comparison of the values of P_{Norm} between RIB-1 with values from Campet et al. [19] and RIB-2.

8. Conclusions

In this article, a numerical flow simulation is successfully validated by measurements. A y^+ value of less than 0.2 is maintained in order to be able to represent the thermal boundary layer as well as the flow boundary layer at a Prandtl number of 7. The local velocity profiles and fluctuations of the velocity between the ribs show a good agreement with the measurements. This proves that the method is capable of reproducing the flow correctly. Using the Nusselt number validation, it can be demonstrated that a maximum Nusselt number is reached between the ribs until the flow reattaches to the wall. This effect is described by Mayo [17] using the RIB-1 geometry and was again observed in this study. Overall heat transfer is reduced compared to the continuous rib, which is proven by both experiment and simulation. The analysis of the wall shear stress showed that the detachment of the flow is shifted further backwards by the interruption, in contrast to the continuous rib. As was previously the case for the flow field, a successful validation is performed for the heat transfer. An analysis of the pressure drop was realized with the help of the results of Campet et al. [19], who performed an LES of the RIB-1 geometry; here, the results could be compared with each other. It could be shown that the C_f value for RIB-2 is higher on the rib than for RIB-1, due to backflow being formed in front of the rib. The pressure coefficient for RIB-2 is lower in comparison to RIB-1, due to the reduction through the rib geometry being interrupted. The simulation was therefore able to reflect the results of the measurement for both the flow and the heat transfer well. Through the results, it can be shown that it is possible to simulate complex internally structured pipes, even without a continuous structure. Thus, further structures with increased complexity can be simulated and evaluated.

Author Contributions: Conceptualization, S.K.; methodology, S.K. and G.O.M.; software, S.K. and G.O.M.; validation, S.K. and P.R.; formal analysis, S.K.; investigation, S.K.; resources, S.K.; data curation, S.K.; writing—original draft preparation, S.K.; writing—review and editing, S.K. and P.R. and T.G.; visualization, S.K.; supervision, P.R. and T.G.; project administration, P.R.; funding acquisition, P.R. All authors have read and agreed to the published version of the manuscript.

Funding: This research was funded by the Federal Ministry of Education and Research of Germany (BMBF) Grant No. 13FH119PX6.

Institutional Review Board Statement: Not applicable.

Informed Consent Statement: Not applicable.

Data Availability Statement: Not applicable.

Acknowledgments: The authors would like to gratefully acknowledge support by the Steinbuch Center for Computing (SCC) at the Karlsruhe Institute of Technology (KIT) for providing computational resources. Most of the simulations have been performed on the bwUniCluster and the forHLR II cluster, where access has been granted to the authors. The article processing charge was funded by the Baden-Württemberg Ministry of Science, Research and the Arts and the University of Applied Sciences Ulm in the funding programme Open Access Publishing.

Conflicts of Interest: The authors declare no conflict of interest.

Abbreviations

The following abbreviations are used in this manuscript:

LES	large-eddy simulation	
RANS	Reynolds-Averaged Navier–Stokes	
OpenFOAM	Open Source Field Operation and Manipulation	
WALE	wall adapting local eddy-viscosity	
S-PIV	stereoscopic particle image velocimetry	
Nu	Nusselt number	
Pr	Prandtl number	
Nomenclature		
t	time	s
$\mathbf{u}$	velocity vector	m/s
U_0	Bulk velocity	m/s
g	gravitational acceleration	m/s^2
k	turbulent kinetic energy	m^2/s^2
P	pressure	Pa
h	enthalpy	J
T	Temperature	K
p	rib pitch	mm
e	rib height	mm
C_f	friction coefficient	-
P_{Norm}	Pressure coefficient	-
Greek symbols		
ρ	density	kg/m^3
μ	dynamic viscosity	$Pa \cdot s$
ν	kinematic viscosity	m^2/s
α	thermal diffusivity	m^2/s
η_{kol}	Kolmogorov length scale	m
τ_x	wall shear stress	m/s^2

References

1. Mousavi Ajarostaghi, S.S.; Zaboli, M.; Javadi, H.; Badenes, B.; Urchueguia, J.F. A Review of Recent Passive Heat Transfer Enhancement Methods. *Energies* **2022**, *15*, 986. [CrossRef]
2. Webb, R.L.; Narayanamurthy, R.; Thors, P. Heat Transfer and Friction Characteristics of Internal Helical-Rib Roughness. *J. Heat Transf.* **1999**, *122*, 134–142. [CrossRef]

3. Gee, D.L.; Webb, R.L. Forced convection heat transfer in helically rib-roughened tubes. *Int. J. Heat Mass Transf.* **1980**, *23*, 1127–1136. [CrossRef]
4. Withers, J.G. Tube-Side Heat Transfer and Pressure Drop for Tubes Having Helical Internal Ridging with Turbulent/Transitional Flow of Single-Phase Fluid. Part 1. Single-Helix Ridging. *Heat Transf. Eng.* **1980**, *2*, 48–58. [CrossRef]
5. Withers, J.G. Tube-Side Heat Transfer and Pressure Drop for Tubes Having Helical Internal Ridging with Turbulent/Transitional Flow of Single-Phase Fluid. Part 2. Multiple-Helix Ridging. *Heat Transf. Eng.* **1980**, *2*, 43–50. [CrossRef]
6. Han, J.; Glicksman, L.; Rohsenow, W. An investigation of heat transfer and friction for rib-roughened surfaces. *Int. J. Heat Mass Transf.* **1978**, *21*, 1143–1156. [CrossRef]
7. Nakayama, M.; Takahashi, K.; Daikoku, T. Spiral ribbing to enhance single-phase heat transfer inside tubes. *Proc. ASME-JSME Therm. Eng. Jt. Conf.* **1983**, *1*, 365–372.
8. Ravigururajan, T.S.; Bergles, A.E. Development and verification of general correlations for pressure drop and heat transfer in single-phase turbulent flow in enhanced tubes. *Exp. Therm. Fluid Sci.* **1996**, *13*, 55–70. [CrossRef]
9. Webb, R.L.; Eckert, E.R.G.; Goldstein, R.J. Heat transfer and friction in tubes with repeated-rib roughness. *Int. J. Heat Mass Transf.* **1971**, *14*, 601–617. [CrossRef]
10. Kumar, P.; Judd, R.L. Heat transfer with coiled wire turbulence promoters. *Can. J. Chem. Eng.* **1970**, *48*, 378–383. [CrossRef]
11. Zdaniuk, G.J.; Chamra, L.M.; Mago, P.J. Experimental determination of heat transfer and friction in helically-finned tubes. *Exp. Therm. Fluid Sci.* **2008**, *32*, 761–775. [CrossRef]
12. Hossainpour, S.; Hassanzadeh, R. Numerical investigation of tub side heat transfer and pressure drop in helically corrugated tubes. *Int. J. Energy Environ. Eng.* **2011**, *2*, 2008–916365.
13. Vijiapurapu, S.; Cui, J. Performance of turbulence models for flows through rough pipes. *Appl. Math. Model.* **2010**, *34*, 1458–1466. [CrossRef]
14. Cauwenberge, D.J.V.; Schietekat, C.M.; Floré, J.; Geem, K.M.V.; Marin, G.B. CFD-based design of 3D pyrolysis reactors: RANS vs. LES. *Chem. Eng. J.* **2015**, *282*, 66–76. [CrossRef]
15. Wang, W.; Zhang, Y.; Liu, J.; Li, B.; Sundén, B. Large eddy simulation of turbulent flow and heat transfer in outward transverse and helically corrugated tubes. *Numer. Heat Transf. Part A Appl.* **2019**, *75*, 456–468. [CrossRef]
16. Akermann, K.; Renze, P.; Dietl, J.; Schröder, W. Large-Eddy Simulation of turbulent heat transfer in a multiple-started helically rib-roughened pipe. *Int. J. Heat Mass Transf.* **2020**, *154*, 119667. [CrossRef]
17. Mayo, I.; Cernat, B.C.; Virgilio, M.; Pappa, A.; Arts, T. Experimental Investigation of the Flow and Heat Transfer in a Helically Corrugated Cooling Channel. *J. Heat Transf.* **2018**, *140*, 071702. [CrossRef]
18. Van Cauwenberge, D.J.; Dedeyne, J.N.; Van Geem, K.M.; Marin, G.B.; Floré, J. Numerical and experimental evaluation of heat transfer in helically corrugated tubes. *AIChE J.* **2018**, *64*, 1702–1713. [CrossRef]
19. Campet, R.; Zhu, M.; Riber, E.; Cuenot, B.; Nemri, M. Large Eddy Simulation of a single-started helically ribbed tube with heat transfer. *Int. J. Heat Mass Transf.* **2019**, *132*, 961–969. [CrossRef]
20. Virgilio, M.; Mayo, I.; Dedeyne, J.; Geem, K.V.; Marin, G.; Arts, T. Effects of 2-D and 3-D helical inserts on the turbulent flow in pipes. *Exp. Therm. Fluid Sci.* **2020**, *110*, 109923. [CrossRef]
21. Virgilio, M.; Mayo, I.; Dedeyne, J.; Geem, K.V.; Marin, G.; Arts, T. Influence of obstacles on the wall heat transfer for 2D and 3D helically ribbed pipes. *Int. J. Heat Mass Transf.* **2020**, *148*, 119087. [CrossRef]
22. Anderson, J. *Computational Fluid Dynamics*; Computational Fluid Dynamics: The Basics with Applications; McGraw-Hill Education: New York, NY, USA, 1995.
23. Ferziger, J.; Peric, M. *Numerische Strömungsmechanik*; Springer: Berlin/Heidelberg, Germany, 2008.
24. Nicoud, F.; Ducros, F. Subgrid-Scale Stress Modelling Based on the Square of the Velocity Gradient Tensor. *Flow Turbul. Combust.* **1999**, *62*, 183–200. [CrossRef]
25. Kügele, S.; Renze, P.; Dietl, J.; Grützner, T. Investigation of heat transfer and pressure drop for a multiple-started ribbed pipe using large-eddy simulation. *AIChE J.* **2022**, e17808. [CrossRef]
26. Pope, S.; Eccles, P. *Turbulent Flows*; Cambridge University Press: Cambridge, UK, 2000.
27. Bergman, T.; Lavine, A.; Incropera, F. *Fundamentals of Heat and Mass Transfer*, 7th ed.; John Wiley & Sons, Incorporated: Hoboken, NJ, USA, 2011.
28. Gnielinski, V. New equations for heat and mass transfer in turbulent pipe and channel flow. *Int. Chem. Eng.* **1976**, *16*, 359–368.